Langmuir
Article

pubs.acs.org/Langmuir

Elastic, Adhesive, and Charge Transport Properties of a Metal−Molecule−Metal Junction: The Role of Molecular Orientation, Order, and Coverage

Frank W. DelRio,*[,†] Kristen L. Steffens,[‡] Cherno Jaye,[†] Daniel A. Fischer,[†] and Robert F. Cook[†]

[†]*Ceramics Division, Materials Science and Engineering Laboratory and* [‡]*Process Measurements Division, Chemical Science and Technology Laboratory, National Institute of Standards and Technology, Gaithersburg, Maryland 20899, USA*

Received July 20, 2009. Revised Manuscript Received September 23, 2009

The elastic, adhesive, and charge transport properties of a metal−molecule−metal junction were studied via conducting-probe atomic force microscopy (AFM) and correlated with molecular structure by near-edge X-ray absorption fine structure (NEXAFS) spectroscopy. The junctions consisted of Co−Cr-coated AFM tips in contact with methyl-terminated alkanethiols ($CH_3(CH_2)_{n-1}SH$, denoted by C_n, where n is the number of carbons in the molecular chain) on Au substrates. AFM contact data were analyzed with the Derjaguin−Muller−Toporov contact model, modified by a first-order elastic perturbation method to account for substrate effects, and a parabolic tunneling model, appropriate for a metal−insulator−metal junction in which the thickness of the insulator is comparable to the Fermi wavelength of the conducting electrons. NEXAFS carbon K-edge spectra were used to compute the dichroic ratio R_I for each film, which provided a quantitative measure of the molecular structure as a function of n. As n decreased from 18 to 5, there was a change in the molecular phase from crystalline to amorphous ($R_I \rightarrow 0$) and loss of surface coverage, and as a result, the work of adhesion w increased from 82.8 mJ m^{-2} to 168.3 mJ m^{-2}, the Young's modulus of the film E_{film} decreased from 1.0 to 0.15 GPa, and the tunneling barrier height $\phi_0 - E_F$ decreased from 2.4 to 2.1 eV. For all n, the barrier thickness t decreased for small applied loads F and remained constant at ∼2.2 nm for large F. The change in behavior was explained by the presence of *two* insulating layers: an oxide layer on the Co−Cr tip, and the alkanethiol monolayer on the Au surface. X-ray photoelectron spectroscopy confirmed the presence of an oxide layer on the Co−Cr tip, and by performing high-resolution region scans through the film, the thickness of the oxide layer t_{oxide} was found to be between 1.9 and 3.9 nm. Finally, it was shown that $\phi_0 - E_F$ is strain-dependent, and the strain at which the film is completely displaced from under the tip is −0.17 for all values of n.

Introduction

Micro-, nano-, and atomic-scale mechanical contacts are anticipated to play a large role as electrical switches and junctions in advanced radio frequency (RF) communications devices,[1,2] nanoelectronics applications,[3] and quantized conductance atomic switches.[4] As an example, the superior performance characteristics of microelectromechanical systems (MEMS)-based switches relative to semiconductor-based switches, including linearity (i.e., Ohmic behavior), small insertion loss and power consumption, small size, and decreased cost, are expected to lead to their use in cellular phones for controlling power, switching between transmit and receive modes, and switching between antenna banks.[1,2,5−7] During operation of an RF MEMS switch, a compliant component of the switch (typically a cantilever) is displaced by electrostatic actuation so as to close an electrical circuit by direct mechanical contact between the device electrodes. Such electrodes have characteristic dimensions of ten to hundreds of micrometers with actuation forces of tens to hundreds of micronewtons, giving rise to contact resistances between 0.1 Ω and 10 Ω (and thus conductances between 10 and 0.1 S). The Ohmic conductance arises from large numbers of metal−metal junctions formed at contacts between subμm-scale asperities on the electrodes. Increased actuation force[5] or sustained[7] and repeated[8,9] loading leads to plastic deformation and flattening of the asperities and greater contact area, resulting in greater contact conductance. For large numbers of loading cycles ($> 10^9$ in some cases),[10] however, the contact area between the electrodes can become so great that adhesion between the electrodes leads to "stiction" and device failure as the electrostatic actuation cannot reopen the switch. In RF MEMS switches, each asperity contact supports a load of ∼1 μN and contributes ∼10 mS to the conductance of the switch. Such contacts are well described by quasi-continuum models of conduction that include diffuse and ballistic electron motion through constrictions.[7,8] At the other extreme, atomic-scale metallic junctions exhibit discrete conductance values quantized in terms of $G_0 = 2e^2/h = 77\,\mu$S, the quantum unit of conductance, where e is the electron charge and h is Planck's constant.[11,12] The characteristic contact load associated with such atomic-scale

*To whom correspondence should be addressed. E-mail: frank.delrio@nist.gov.

(1) Yao, J. J. *Micromech. Microeng.* **2000**, *10*, R9.
(2) Tilmans, H. A. C.; De Raedt, W.; Beyne, E. J. *Micromech. Microeng.* **2003**, *13*, S139.
(3) Cui, Y.; Lieber, C. M. *Science* **2001**, *291*, 851.
(4) Terabe, K.; Hasegawa, T.; Nakayama, T.; Aono, M. *Nature* **2005**, *433*, 47.
(5) Hyman, D.; Mehregany, M. *IEEE Trans. Compon., Packag. Technol.* **1999**, *22*, 357.
(6) Mercado, L. L.; Kuo, S. -M.; Lee, T. -Y. T.; Liu, L. *Electron. Compon. Technol. Conf.* **2003**, 377.
(7) Patton, S. T.; Zabinski, J. S. *Trib. Lett.* **2005**, *18*, 215.
(8) Majumder, S.; McGruer, N. E.; Adams, G. G.; Zavracky, P. M.; Morrison, R. H.; Krim, J. *Sens. Actuators A* **2001**, *93*, 19.
(9) Gregori, G.; Clarke, D. R. *J. Appl. Phys.* **2006**, *100*, 094904.
(10) Newman, H. S.; Ebel, J. L.; Judy, D.; Maciel, J. *IEEE Microwave Compon. Lett.* **2008**, *18*, 100.
(11) Pascual, J. I.; Mendez, J.; Gomez-Herrero, J.; Baro, A. M.; Garcia, N.; Landman, U.; Luedtke, W. D.; Bogachek, E. N.; Cheng, H. -P. *J. Vac. Sci. Technol. B* **1995**, *13*, 1280.
(12) Hansen, K.; Nielsen, S. K.; Brandbyge, M.; Laegsgaard, E.; Stensgaard, I.; Besenbacher, F. *Appl. Phys. Lett.* **2000**, *77*, 708.

junctions is ~1 nN, the force required to break a single atomic bond.

Nanoelectromechanical systems (NEMS) switches and junctions will utilize contact loads between the ~1 μN of MEMS devices and the ~1 nN of atomic-scale junctions, and in this range, electrical behavior may depend on the mechanical loading: the small contact loads may not be able to induce plasticity at the contact and thus establish metal−metal junctions, and yet the contacts will be much larger than the atomic scale required for quantized conductance. An early study by Tonck et al. revealed the essential features of the electrical and mechanical coupling at nanoscale contacts: the conductance values of nominally Au−Au contacts were significantly less than G_0, typically $0.01G_0$; the current (I)−voltage (V) characteristics were markedly nonlinear but symmetric about zero bias; and the $I-V$ behavior depended significantly on the contact load, with increasing load (and decreasing contact separation) leading to increased conductance.[13] The behavior was well modeled[13,14] using a multiasperity description of the surfaces[14] and electron tunneling through an adventitious, insulating layer between the surfaces as the charge transport limiting mechanism. Further studies using ultrahigh vacuum (UHV) conducting-probe atomic force microscopy (AFM) or related techniques of metal−metal[15−20] and metal−semiconductor[16,21] nanoscale contacts, in which the insulating barrier material was either adventitious[15,17,18,20] or deliberately formed using an organic molecular film,[15,19] revealed similar behavior: extremely small conductance values and nonlinear $I-V$ behavior indicative of a tunneling mechanism.

For nanoscale metallic junctions with organic molecular interlayers, several studies have shown that the exact details regarding the mechanical and electrical behavior of the contact are dependent on the molecular composition (e.g., hydrocarbon vs fluorocarbon chain, thiol vs silane headgroup) and order (e.g., densely packed, crystalline-like vs loosely packed, liquid-like). Lio et al. studied the frictional properties of alkanethiol and alkylsilane monolayers as a function of the chain length, or number of carbon atoms in the molecular chain, n.[22] For $n > 11$, the thiols and silanes displayed similar frictional behavior, independent of chain length and headgroup linkage, due to the densely packed, invariant structure of the films. For $n < 11$, however, the frictional trends were dependent on the chain length and headgroup, with larger values reported for the silanes and decreasing n, presumably from increased disorder from numerous defects and energy-dissipating modes. Boulas et al. conducted photoconductivity experiments at variable excitation wavelengths to extract the band gaps for several long-chain (n = 12, 16, and 18) alkylsilane monolayers.[23] The band gap was found to be independent of n for the densely packed, crystalline-like monolayers, but decreased significantly for similar liquid-like films with only partial surface coverage. In these (and most other) studies, information regarding molecular structure is typically inferred via *qualitative* techniques such as Fourier transform infrared spectroscopy. In a recent report, however, Sambasivan et al. utilized near-edge X-ray absorption fine structure (NEXAFS) spectroscopy to *quantitatively* link molecular orientation to frictional behavior of alkylsilane monolayers.[24] DelRio et al. conducted similar experiments to investigate the work of adhesion and elastic modulus of alkanethiols.[25] In both studies, the trends were interpreted in terms of the dichroic ratios, which revealed distinct changes in molecular structure.

In this paper, the elastic, adhesive, and charge transport properties of methyl-terminated alkanethiols ($CH_3(CH_2)_{n-1}SH$, denoted by C_n) on Au are examined via AFM and correlated with molecular structure by NEXAFS spectroscopy. AFM contact data are analyzed with the Derjaguin−Muller−Toporov (DMT) contact model,[26,27] modified to extract the film modulus by a first-order elastic perturbation method to account for substrate effects,[28] and a parabolic tunneling-barrier conductance model, appropriate for a metal−insulator−metal contact in which the insulator is extremely thin.[29] NEXAFS carbon K-edge spectra are used to compute the dichroic ratio for each film, which provides a quantitative measure of the molecular structure. The combination of the two measurement methods provides a structure−property relationship for this particular system over a wide range of n and a general methodology for the optimization of self-assembled monolayers for MEMS, magnetic storage, and other applications.

Theoretical Background

Elastic Adhesive Contact. The link between contact mechanics and interfacial adhesion has been studied for some time now. Johnson, Kendall, and Roberts (JKR) developed a model to predict the deformed shape of two contacting spheres (radii R_1 and R_2) that interact via attractive surface forces based on a balance between elastic energy and surface energy.[30] To simplify the analysis, it is convenient to consider the case of a rigid sphere in contact with an elastic half-space. Under an applied load F, the rigid sphere deforms the flat surface a distance δ to form a contact over a circle of radius a, given by

$$F = \frac{4E^*a^3}{3R} - 2\sqrt{2\pi E^* w a^3} \tag{1}$$

and

$$\delta = \frac{a^2}{R} - \sqrt{\frac{2\pi a w}{E^*}} \tag{2}$$

where w is the work of adhesion, E^* is the reduced modulus of the contact, and R is the radius of the rigid sphere. Here, the reduced modulus is the plane strain modulus of the linear-elastic, isotropic half-space, $E^* = E/(1-\nu^2)$, where E and ν are the Young's modulus and Poisson's ratio, respectively. From eqs 1 and 2, we

(13) Tonck, A.; Houze, F.; Boyer, L.; Loubet, J. -L; Georges, J. -M. *J. Phys.: Condens. Matter* **1991**, *3*, 5195.
(14) Houze, F.; Boyer, L. *J. Phys.: Condens. Matter* **1991**, *3*, 4655.
(15) Beale, J.; Pease, F. *IEEE Trans. Compon. Packag. Manuf. Technol. A* **1994**, *17*, 257.
(16) Lantz, M. A.; O'Shea, S. J.; Welland, M. E. *Phys. Rev. B* **1997**, *56*, 15345.
(17) Tringe, J. W.; Uhlman, T. A.; Oliver, A. C.; Houston, J. E. *J. Appl. Phys.* **2003**, *93*, 4661.
(18) Enachescu, M.; Carpick, R. W.; Ogletree, D. F.; Salmeron, M. *J. Appl. Phys.* **2004**, *95*, 7694.
(19) Qi, Y.; Ratera, I.; Park, J. Y.; Ashby, P. D.; Quek, S. Y.; Neaton, J. B.; Salmeron, M. *Langmuir* **2008**, *24*, 2219.
(20) Kim, D.-I.; Pradeep, N.; DelRio, F. W.; Cook, R. F. *Appl. Phys. Lett.* **2008**, *93*, 203102.
(21) Enachescu, M.; van der Oetelaar, R. J. A.; Carpick, R. W.; Ogletree, D. F.; Flipse, C. F. J.; Salmeron, M. *Phys. Rev. Lett.* **1998**, *81*, 1877.
(22) Lio, A.; Charych, D. H.; Salmeron, M. *J. Phys. Chem. B* **1997**, *101*, 3800.
(23) Boulas, C.; Davidovits, J. V.; Rondelez, F.; Vuillaume, D. *Phys. Rev. Lett.* **1996**, *76*, 4797.
(24) Sambasivan, S.; Hsieh, S.; Fischer, D. A.; Hsu, S. M. *J. Vac. Sci. Technol. A* **2006**, *24*, 1484.
(25) DelRio, F. W.; Jaye, C.; Fischer, D. A.; Cook, R. F. *Appl. Phys. Lett.* **2009**, *94*, 131909.
(26) Derjaguin, B. V.; Muller, V. M.; Toporov, Y. P. *J. Colloid Interface Sci.* **1975**, *53*, 314.
(27) Muller, V. M.; Derjaguin, B. V.; Toporov, Y. P. *Colloids Surf.* **1983**, *7*, 251.
(28) Xu, H.; Pharr, G. M. *Scr. Mater.* **2006**, *55*, 315.
(29) Hansen, K.; Brandbyge, M. *J. Appl. Phys.* **2004**, *95*, 3582.
(30) Johnson, K. L.; Kendall, K.; Roberts, A. D. *Proc. R. Soc. London, A* **1971**, *324*, 301.

see that the contact area $A = \pi a^2$ is larger than that predicted by the Hertz theory,[31] and remains finite until a critical pull-off force is reached, at which point the surfaces separate abruptly. In a load-controlled system, such as a compliant AFM cantilever, the pull-off force is reached at $-3\pi Rw/2$. At pull-off, the sphere does not separate from the flat surface at the same position in which it came into contact. In fact, the contact is elongated to a pull-off distance of $-(3\pi^2 w^2 R/64E^{*2})^{1/3}$.

Derjaguin, Muller, and Toporov used a completely different approach to consider the molecular forces in an annular zone around the area of contact.[26,27] Unlike the JKR model, the profile of the contact is assumed to be Hertzian. Originally, using a "thermodynamic" approach, Derjaguin et al. found that, at initial contact, the attractive force between the sphere and flat surface is $2\pi Rw$, but as the deformation increases, this force decreases rapidly to πRw.[26] However, as the contact deforms, the adhesive force should become larger, not smaller, than $2\pi Rw$. Muller et al. eventually developed a model consistent with this idea using a more correct "force" method.[27] In the revised model, the attractive force is again $2\pi Rw$ at contact, but this time increases as the sphere and flat are pressed closer together according to

$$F = \frac{4E^* a^3}{3R} - 2\pi Rw \tag{3}$$

and

$$\delta = \frac{a^2}{R} \tag{4}$$

At $\delta = 0$, the sphere and flat surface separate at the initial point of contact, and eq 3 reduces to the Bradley solution for a rigid sphere in contact with a rigid flat surface.[32]

At first glance, the JKR and DMT models seem to contradict each other: the pull-off force in the former case is $-3\pi Rw/2$, while the pull-off force in the latter case is $-2\pi Rw$. Tabor compared the two models, and briefly outlined some of the problems associated with each of the solutions.[33] In the JKR theory, the adhesive forces outside the area of contact are neglected. These forces, however, must be taken into account when the height h of the "neck" around the contact, which is given by $(Rw^2/E^{*2})^{1/3}$, approaches the equilibrium separation z_0. The DMT model includes the adhesive forces along the periphery, but assumes the contact profile is Hertzian in nature (i.e., the surface forces are small enough that their effect on the deformation can be neglected). Muller et al. performed a numerical calculation based on the Lennard-Jones potential and determined the models actually represent the extreme ends of a spectrum defined by the parameter[34]

$$\mu = \left(\frac{Rw^2}{E^{*2} {z_0}^3}\right)^{1/3} \tag{5}$$

which represents the ratio of elastic deformation to the effective range of surface forces. Thus, the JKR theory is suitable for compliant materials with large, short-range surface forces ($\mu \gg 1$), while the DMT theory is appropriate for stiff contacts with small, long-range attractive forces ($\mu \ll 1$). The $F-\delta$ relationships

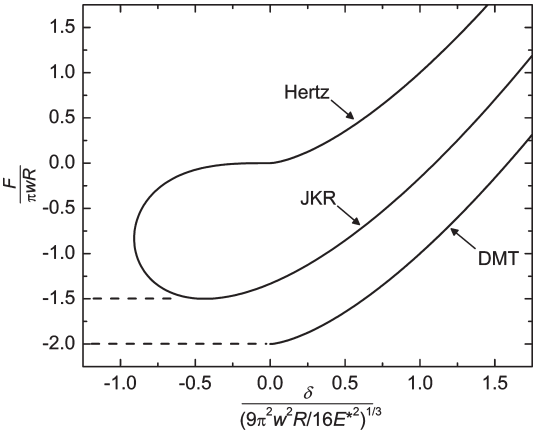

Figure 1. Normalized $F-\delta$ curves for the JKR and DMT elastic adhesive contact models. In the absence of adhesion, both models approach the Hertzian case.

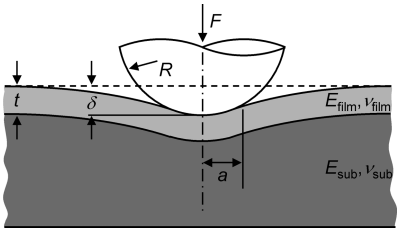

Figure 2. Schematic diagram of a rigid sphere in contact with a coated elastic half space.

for the JKR and DMT contact models are shown in Figure 1. As $w \rightarrow 0$, both models converge to the Hertz theory.

Effective Elastic Modulus of a Film−Substrate System. As previously mentioned, for a rigid sphere in contact with a linear-elastic, isotropic flat surface, $E^* = E/(1-\nu^2)$. On the other hand, when the flat surface is a thin film of thickness t on a substrate, as shown in Figure 2, E^* is a function of the Young's moduli and Poisson's ratios of the film (E_{film}, ν_{film}) *and* the substrate (E_{sub}, ν_{sub}). Therefore, to find the "true" film properties, it becomes necessary to either limit δ to avoid substrate effects or fit the experimental data to a film−substrate model. In the former approach, a common rule of thumb to measure *hardness* is to limit the deformation to $\delta = 0.10t$, because, beyond this depth, the plastic zone beneath the interface reaches the substrate and affects the measured film properties.[35] This is not a comprehensive law, however, as the size of the plastic zone at a given δ depends on the film/substrate hardness ratio and the indenter geometry.[36,37] In determining *elastic* film properties, the extracted values are even more sensitive to the substrate as a result of the long-range nature of the elastic field under the point of contact, with substrate-dependent properties starting at $\delta = 0.05t$.[37] For thin films, it is clear that these guidelines can severely limit the experimental measurement range. As a consequence, it is useful to consider the latter option, which involves fitting the experimental data to an empirical[38,39] or analytical[40−42] model. The model by Gao et al. is

(31) Hertz, H. *J. Reine Angew. Math.* **1881**, *92*, 156.
(32) Bradley, R. S. *Philos. Mag.* **1932**, *13*, 853.
(33) Tabor, D. *J. Colloid Interface Sci.* **1977**, *58*, 2.
(34) Muller, V. M.; Yushenko, V. S.; Derjaguin, B. V. *J. Colloid Interface Sci.* **1980**, *77*, 91.
(35) Buckle, H. *The Science of Hardness Testing and Its Research Applications*; Westbrook, J W, Conrad, H., Eds.; American Society for Materials: Materials Park, OH, 1973.
(36) Lebouvier, D.; Gilormini, P.; Felder, E. *Thin Solid Films* **1989**, *172*, 227.
(37) Saha, R.; Nix, W. D. *Acta Mater.* **2002**, *50*, 23.
(38) Doerner, M. F.; Nix, W. D. *J. Mater. Res.* **1986**, *1*, 601.
(39) King, R. B. *Int. J. Solids Struct.* **1988**, *23*, 1657.
(40) Gao, H.; Chiu, C.-H.; Lee, J. *Int. J. Solids Struct.* **1992**, *29*, 2471.
(41) Yoffe, E. H. *Philos. Mag. Lett.* **1998**, *77*, 69.
(42) Perriot, A.; Barthel, E. *J. Mater. Res.* **2004**, *19*, 600.

particularly useful due to its simple, closed-form solution.[40] The analysis, which is based on a first-order elastic perturbation method, is in good agreement with finite element modeling for films and substrates with similar elastic properties. However, in the rigid substrate limit (i.e., $E_{sub} \rightarrow \infty$), the model predicts that E^* depends solely on E_{sub} and not E_{film}, which is clearly incorrect and leads to large errors when $E_{sub} \gg E_{film}$. Xu and Pharr improved the model for this case via a simple modification to the first-order perturbation approximation.[28] In the revised model, the effective elastic modulus is given by

$$\frac{1}{E^*} = \frac{1}{2}[1-\nu_{sub}+(\nu_{sub}-\nu_{film})I_1]\left[\frac{2(1+\nu_{sub})}{E_{sub}}(1-I_0)+\frac{2(1+\nu_{film})}{E_{film}}I_0\right] \quad (6)$$

where

$$I_0(\xi) = \frac{2}{\pi}\arctan\xi + \frac{1}{2\pi(1-\nu_{sub})}\left[(1-2\nu_{sub})\xi\ln\frac{1+\xi^2}{\xi^2} - \frac{\xi}{1+\xi^2}\right] \quad (7)$$

and

$$I_1(\xi) = \frac{2}{\pi}\arctan\xi + \frac{\xi}{\pi}\ln\frac{1+\xi^2}{\xi^2} \quad (8)$$

are weighting functions that account for shear modulus mismatch and Poisson's ratio effects, respectively, and depend on the normalized film thickness, $\xi = t/a$. For $E_{sub} > E_{film}$, eq 6 is found to yield results within 10% of those obtained with finite element models over a wide range of E_{film}/E_{sub}. It is important to point out that the modification to the perturbation method leads to inaccuracies in the rigid film limit. As $E_{film} \rightarrow \infty$, the model predicts a nonzero value for E^*. This should not be an issue in this particular study, however, as the alkanethiol films are expected to be much more compliant than the Au substrate.

Electron Tunneling Through Thin Insulating Films. The link between the mechanical and electrical behavior of a metal−metal junction is through the contact radius a. $I-V$ curves are measured at different values of F and the measured variation of the conductance ($G = I/V$) with a compared with predictions from contact mechanics models for the variation of a with F. The relationship between G and a can take on various forms depending on the principle conduction mechanism, which can be defined by comparing a to both the mean free path l and the Fermi wavelength λ_F of the conducting electrons. For a macroscopic contact ($a > l$), the conductance is due to diffusive transport and is described by the Maxwell conductance[43] $G_M = 2a\sigma$, where σ is the conductivity of the two metals in contact. For smaller contacts ($a < l$), the conductance is due to ballistic transport and is described by the Sharvin conductance[44] $G_S = (\pi a/\lambda_F)^2 G_0$. When $a \approx l$, the transition from G_M to G_S can be described in terms of an interpolation function.[45] As a becomes smaller and comparable to λ_F, G approaches the fundamental limit G_0. For alkaline and noble metals, the conductance is quantized around integer values of G_0, whereas for other metals, the conductance is not quantized.[46]

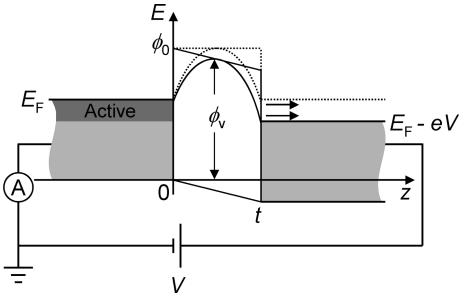

Figure 3. Schematic diagram of the electron energy levels in a metal−insulator−metal structure in which the insulator forms a parabolic barrier for electron tunneling between the metals. The dotted and solid lines indicate the levels in the unbiased and biased state, respectively.

Regardless of the metals in question, when they are in intimate contact, it is clear that G can not be less than G_0.

On the other hand, when the metal−metal junction is separated by a thin insulating layer, such as an adventitious hydrocarbon[15,17,18,20] or a deliberately formed organic monolayer,[15,19] the conductance values are significantly less than G_0. Wang et al. demonstrated that the dominant conduction mechanism through alkanethiols is in fact direct, nonresonant tunneling when the applied voltage is less than the barrier height.[47] A number of analytical expressions have been developed to describe the $I-V$ characteristics of metal−insulator−metal tunneling junctions.[48−50] The derivations are commonly based on the Wentzel−Kramers−Brillouin (WKB) approximation, which is a semiclassical method for obtaining an approximate solution to the Schrödinger equation. However, the WKB approach is valid only when t is much greater than λ_F, which ranges from 0.5 to 1 nm for most metals.[51] As t approaches λ_F, which is often the case for organic monolayers, the validity of the WKB approximation comes into question.

Hansen and Brandbyge developed a different approach to describe the $I-V$ characteristics of metal−insulator−metal tunneling junctions.[29] The method assumes a parabolic shape for the tunneling barrier; an energy diagram for a parabolic tunneling barrier is shown in Figure 3. In the unbiased state, $V = 0$, the Fermi energies E_F of the two electrodes are at the same energy level E, whereas in the biased state, the Fermi levels are offset by eV, which enables electrons to travel from left to right through the tunneling barrier. The general formula for current due to tunneling is given by

$$I = G_S T_m(V) V = \left(\frac{\pi a}{\lambda_F}\right)^2 G_0 T_m(V) V \quad (9)$$

where $T_m(V)$ is the mean transmission probability averaged over all electrons. For very thin barriers and at small voltages, $T_m(V) \approx 1$. Thus, at this extreme, the $I-V$ behavior is described solely in terms of the Sharvin conductance, or by $I = G_S V$. The transition to the Sharvin behavior is appropriate, as the contact radius at each load is much less than the mean free path, which is on the order of 10 nm for metals at room temperature.[51] In the presence of a realistic barrier, however, $T_m(V) \ll 1$. With the Sommerfeld expansion,[51] $T_m(V) \sim T_0(V) + \Delta T(V)$, where $T_0(V)$

(43) Maxwell, J. C. *A Treatise on Electricity and Magnetism*; Oxford University Press: London, 1892.
(44) Sharvin, Y. V. *Zh. Eksp. Teor. Fiz.* **1965**, *48*, 984.
(45) Nikolic, B.; Allen, P. B. *Phys. Rev. B* **1999**, *60*, 3963.
(46) Ludoph, B.; van Ruitenbeek, J. M. *Phys. Rev. B* **2000**, *61*, 2273.
(47) Wang, W.; Lee, T.; Reed, M. A. *Phys. Rev. B* **2003**, *68*, 035416.
(48) Stratton, R. *J. Phys. Chem. Solids* **1962**, *23*, 1177.
(49) Simmons, J. G. *J. Appl. Phys.* **1963**, *34*, 1793.
(50) Simmons, J. G. *J. Appl. Phys.* **1963**, *34*, 2581.
(51) Ashcroft, N. W.; Mermin, N. D. *Solid State Physics*; Holt, Rinehart and Winston: New York, 1976.

is the zero temperature mean transmission and $\Delta T(V)$ is the temperature correction. Using the extended parabolic barrier model,[29]

$$T_0(V) = \frac{1}{\gamma^2 E_F e V}(\mathrm{Li}_2\{-\exp[-\gamma(eV+\phi_V-E_F)]\} - \mathrm{Li}_2\{-\exp[-\gamma(\phi_V-E_F)]\}) \quad (10)$$

and

$$\Delta T(V) = \frac{\pi^2}{6}\frac{(k_B T)^2}{E_F e V}\left\{\frac{1}{1+\exp[\gamma(\phi_V-E_F)]} - \frac{1}{1+\exp[\gamma(eV+\phi_V-E_F)]}\right\} \quad (11)$$

where $\mathrm{Li}_2(z)$ is the dilogarithm function, k_B is Boltzmann's constant, T is the temperature, $\gamma = (\pi^2 t/h)(2m/\phi_0)^{1/2}$, $\phi_V = \phi_0(1 - eV/4\phi_0)^2$ is the voltage-dependent maximum barrier height, m is the mass of an electron, and ϕ_0 is the zero bias barrier height. In a metal−molecule−metal junction, $\phi_0 - E_F$ corresponds to the energy difference between the Fermi level of the metal and the nearest molecular orbital (i.e., the tunneling barrier height), while t corresponds to the thickness of the molecule. Engelkes et al. showed that the nearest molecular orbital for alkanethiol films is the highest occupied molecular orbital (HOMO), as opposed to the lowest unoccupied molecular orbital (LUMO).[52] In other words, $\phi_0 - E_F$ could be rewritten as $E_F - E_{HOMO}$, where E_{HOMO} is the energy level of the highest occupied molecular orbital. However, to stay true to the original nomenclature, the barrier height will be denoted as $\phi_0 - E_F$.

Experimental Methods

Sample Preparation. Alkanethiols (n = 5, 8, 12, and 18) and Si(100) wafers coated with a 5 nm Ti adhesion layer followed by a 100 nm Au film were purchased from Sigma-Alrich (Milwaukee, WI). The alkanethiols were used as received, and the Au-coated Si wafers were cut into 6 mm × 6 mm samples. The samples were cleaned with piranha solution (3:1 H_2SO_4:H_2O_2), immersed in 1 mM ethanolic solutions of the alkanethiols for 24 h, rinsed in pure ethanol, dried under a N_2 flow, and stored in UHV for at least a week to allow for monolayer diffusion and ripening.[53] Prior to the NEXAFS and AFM studies, some of the samples were examined via goniometry and spectroscopic ellipsometry to ensure monolayer formation. The advancing and receding water contact angles (θ_a, θ_r) were measured with goniometry using the sessile drop technique. For n = 5, 8, 12, and 18, θ_a = 88°, 101°, 104°, and 107° and θ_r = 73°, 95°, 99°, and 101°, respectively. The values and trends are consistent with previous studies, which illustrate smaller contact angles for decreasing n, presumably due to substrate effects or disorder in the short-chain molecules.[54] The thickness t of each monolayer was determined by spectroscopic ellipsometry, assuming a refractive index[55] of n_f = 1.50. The average values of t for n = 5, 8, 12, and 18 were found to be 0.38, 0.74, 1.25, and 2.03 nm, respectively. Again, the values are consistent with previous results for alkanethiol monolayers.[54,56] For n = 18, the measured value is nearly equivalent to the theoretical length of the molecule tilted 30° from the surface normal. However, as n decreases, the observed values fall below theoretical calculations. The variation is attributed to smaller packing densities, which lead to smaller refractive indexes and thus smaller measured thicknesses.

Near-Edge X-ray Absorption Fine Structure Spectroscopy. NEXAFS measurements were carried out at the NIST U7A beamline of the National Synchrotron Light Source. Partial electron yield (PEY) spectra at the carbon K-edge, 270 to 330 eV (1 eV = 1.6 × 10^{-19} J), were obtained with a channeltron retarding voltage of −225 V to enhance the surface sensitivity and Auger yield. Drain currents of a carbon mesh and a clean gold mesh, both located in the path of the incident, linearly polarized photon beam, were measured to aid in energy calibration and normalization of the PEY signal, respectively. NEXAFS spectra were taken at angles θ ranging from 20° to 90°, measured between the sample surface and the photon beam.

Atomic Force Microscopy. AFM experiments were performed in UHV (base pressure 5 × 10^{-8} Pa) with an RHK Technology (Troy, MI) UHV 3000 scanning probe microscope. Si cantilevers coated with 60 nm of Co followed by 20 nm of Cr (NSC36/Co−Cr) from Mikromasch (San Jose, CA) were used for the mechanical and electrical measurements. Cantilever spring constants in the normal direction k were determined by the thermal fluctuation method;[57] values for k were found to vary between 2.3 N m^{-1} and 3.3 N m^{-1}. The probe tips were inspected before and after contact experiments to check for damage with scanning electron microscopy. The average tip radius was found to be ∼20 nm, with no discernible changes due to contact. The probe was grounded and the sample bias was controlled during the experiments. Displacement d of the cantilever toward the sample surface led to unstable "snap-on" of the tip to the surface on approach followed by compressive contact to a peak load. Retraction of the cantilever led to an *almost* reversible decrease of the compressive load, followed by a stable, increasing tensile load as the tip adhered to the surface, and finally unstable "pull-off" of the tip from the surface. At various points in the extension and retraction cycle, cantilever displacement was halted, and $I-V$ measurements were performed. The sample bias was swept from −2 V to +2 V in about 2 s and the current recorded. The upper bound on the current measurement was 100 nA, set by the saturation of the current amplifier.

X-ray Photoelectron Spectroscopy (XPS). XPS measurements were performed in UHV on a Kratos Analytical (Chestnut Ridge, NY) Axis Ultra DLD spectrometer with a monochromated Al Kα source at a 0° angle between the sample surface normal and the analyzer lens. Survey spectra were collected with a source power of 150 W and a 110 μm aperture. The pass energy was 160 eV with a 0.5 eV step size. Depth profiling was accomplished by sputtering a 4 mm × 4 mm section of the surface with a 4 kV, 50 μA extractor current argon beam in 10 s increments near the surface and then 20 s increments. At each depth, high-resolution spectra were obtained for the O 1s, C 1s, Si 2p, Cr 2p, and Co 2p regions with a source power of 140 W using a hybrid lens and a "slot" (∼300 μm × 700 μm) aperture. The pass energy was 40 eV with a 0.1 eV step size. XPS spectra were analyzed using CasaXPS (Bend, OR), version 2.3.12.

Results and Discussion

Molecular Orientation, Order, and Coverage. NEXAFS PEY spectra at the carbon K-edge for n = 5, 8, 12, and 18 at θ = 20°, 44°, and 70° are shown in Figure 4a. All spectra exhibit the same characteristic hydrocarbon resonance peaks: the C=C π^* peak at 285.5 eV, the C−H σ^* peak at 288.6 eV, and the C−C σ^* peak at 293.6 eV. For n = 5 and 8, the spectra are nearly identical. However, n = 12 and 18 reveal a strong angular dependence, with

(52) Engelkes, V. B.; Beebe, J. M.; Frisbie, C. D. *J. Am. Chem. Soc.* **2004**, *126*, 14287.
(53) Barrena, E.; Ocal, C.; Salmeron, M. *J. Chem. Phys.* **1999**, *111*, 9797.
(54) Bain, C. D.; Troughton, E. B.; Tao, Y. -T.; Evall, J.; Whitesides, G. M.; Nuzzo, R. G. *J. Am. Chem. Soc.* **1989**, *111*, 321.
(55) Ulman, A. *An Introduction to Ultrathin Organic Films: From Langmuir-Blodgett to Self-Assembly*; Academic Press: New York, 1991.
(56) Porter, M. D.; Bright, T. B.; Allara, D. L.; Chidsey, C. E. D. *J. Am. Chem. Soc.* **1987**, *109*, 3559.
(57) Hutter, J. L.; Bechhoefer, J. *Rev. Sci. Instrum.* **1993**, *64*, 1868.

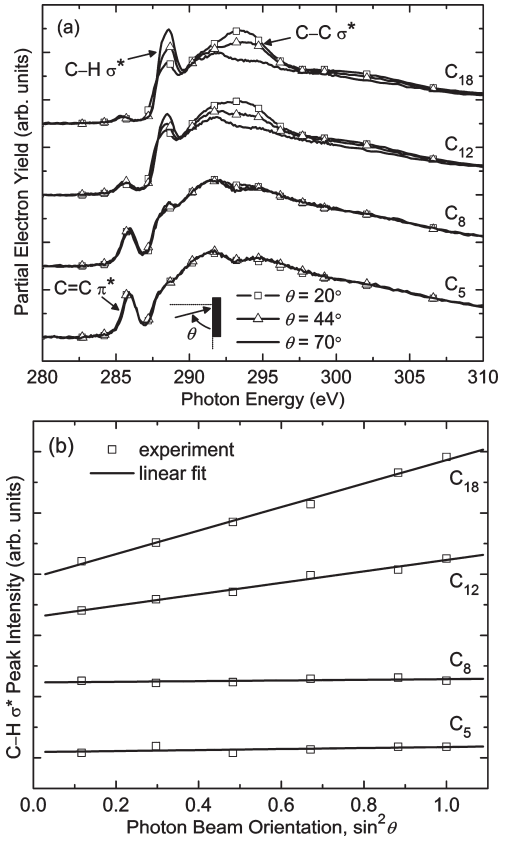

Figure 4. (a) NEXAFS carbon *K*-edge PEY spectra for $n = 5$, 8, 12, and 18 at various θ (offset for clarity). For $n = 5$ and 8, the spectra are identical. However, $n = 12$ and 18 reveal a strong angular dependence, with C−H σ^* resonance decreasing and C−C σ^* resonance increasing as θ decreases. (b) NEXAFS C−H σ^* peak intensities versus $\sin^2\theta$ for $n = 5$, 8, 12, and 18 (offset for clarity).

C−H σ^* resonance decreasing and C−C σ^* resonance increasing as θ decreases. Also, as n decreases, the intensity of the C=C π^* resonance peak increases, likely the result of small surface coverage and the subsequent deposition of adventitious hydrocarbons on the Au surface for the short-chain molecules. The peak intensities were quantified by fitting Gaussian peaks to the spectra and integrating the peak areas;[58] the resulting C−H σ^* peak intensities are plotted as a function of $\sin^2\theta$, as shown in Figure 4b. The variations in peak intensity with θ are related to the molecular orientation through the dichroic ratio $R_I = (I_{90°} - I_{0°})/(I_{90°} + I_{0°})$, where $I_{90°}$ is the peak intensity at $\theta = 90°$ and $I_{0°}$ is the extrapolated peak intensity at $\theta = 0°$. R_I can vary from −1 to +0.75, with a more positive value for the C−H σ^* plane corresponding to greater surface normality ($R_I = 0$ may also represent a random distribution of chain orientations).[24] Table 1 summarizes the C−H σ^* dichroic ratios. For $n = 18$, $R_I = 0.50$, indicative of a densely packed, crystalline-like film. As n decreases, R_I decreases; by definition, this indicates an increase in *average* tilt angle and change in phase from crystalline to amorphous. The trends here are consistent with electron diffraction experiments, which suggest that long-chain ($n \geq 9$) alkanethiols form densely packed, crystalline-like monolayers with $(\sqrt{3} \times \sqrt{3})$ $R30°$ molecular periodicity,[59,60] while short-chain alkanethiols result in loosely packed, liquid-like films with $(m\sqrt{3} \times \sqrt{3})$ $R30°$ surface structure (where m varies from 1 to 6 depending on n).[60]

Table 1. Dichroic Ratio R_I, Work of Adhesion w, Young's Modulus E_{film}, Barrier Height $\phi_0 - E_F$, and Viscoelastic-Plastic Deformation δ_p for $n = 5$, 8, 12, and 18

n	R_I C−H σ^{*a}	w (mJ m^{-2})^b	E_{film} (GPa)^b	$\phi_0 - E_F$ (eV)^b	δ_p (nm)^a
5	0.04 ± 0.04	168.3 ± 17.6	0.15 ± 0.04	2.10 ± 0.26	0.38 ± 0.01
8	0.02 ± 0.02	125.4 ± 9.0	0.28 ± 0.08	2.17 ± 0.30	0.40 ± 0.01
12	0.26 ± 0.02	104.1 ± 9.8	0.86 ± 0.14	2.25 ± 0.15	0.70 ± 0.04
18	0.50 ± 0.03	82.8 ± 9.0	1.00 ± 0.18	2.39 ± 0.35	0.40 ± 0.04

[a] Uncertainty values represent a 95% confidence level in the fit. [b] Or two standard deviations from at least five measurements.

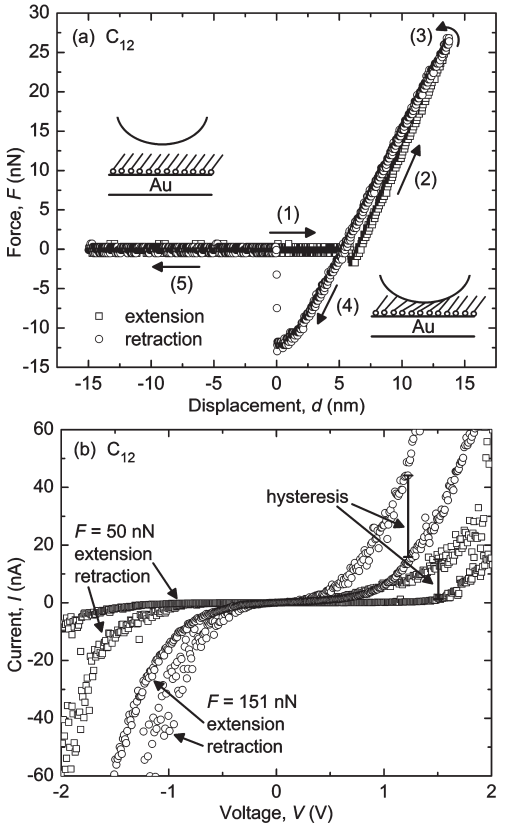

Figure 5. (a) $F-d$ experimental data for $n = 12$. The $F-d$ data includes both the extension of the cantilever toward the sample surface (1, 2) to a peak load (3) and the retraction of the cantilever away from the sample surface (4, 5). The schematic diagrams illustrate the deformation state of the monolayer at various stages. (b) $I-V$ traces during extension and retraction of the cantilever at $F = 50$ nN and $F = 151$ nN.

Elastic and Adhesive Properties. AFM $F-d$ data for $n = 12$ are shown in Figure 5a. The $F-d$ data includes both the extension (loading) of the cantilever toward the sample surface to a peak load and the retraction (unloading) of the cantilever away from the sample surface. At various points in the extension and retraction cycle, cantilever displacement was halted and $I-V$ measurements performed as shown in Figure 5b. The hysteresis in the $F-d$ data is most likely from the "reverse-path" effect, which is due to hysteresis and creep in the piezoactuator used to control the displacement of the AFM cantilever.[61] This nonideal behavior

(58) Outka, D. A.; Stöhr, J.; Rabe, J. P.; Swalen, J. D. *J. Chem. Phys.* **1988**, *88*, 4076.
(59) Strong, L.; Whitesides, G. M. *Langmuir* **1988**, *4*, 546.
(60) Dubois, L. H.; Zegarski, B. R.; Nuzzo, R. G. *J. Chem. Phys.* **1993**, *98*, 678.
(61) Hues, S. M.; Draper, C. F.; Lee, K. P.; Colton, R. J. *Rev. Sci. Instrum.* **1994**, *65*, 1561.

causes the retraction curve to pass over the extension curve. In other words, at a given d, F is greater on unloading than on loading. This phenomenon, however, would not explain the hysteresis in the $I-V$ data, because the curves were taken at the same values of F (not d) on loading and unloading. Other mechanisms that would explain the $I-V$ hysteresis include adhesion hysteresis, viscoelastic effects, and plastic deformation. A change in the adhesion energy during loading and unloading might be responsible for the observed hysteresis. Schneider et al. noted hysteresis in the adhesion energy of glycine amphiphile bilayers by surface-force apparatus experiments.[62] The hysteresis was attributed to a spatially varying adhesion gradient in the contact zone due to pH-dependent surface rearrangement from the snap-on of the tip to the surface. At high pH, both the adhesion and adhesion hysteresis disappeared, which provided further evidence for the spatially varying adhesion gradient model and ensured the deformation was purely elastic. Similar experiments with alkanethiol monolayers, however, tell a different story.[63] In the absence of adhesion, which was achieved via measurements in solution, the hysteresis was still observed and therefore not due to adhesive effects. Another possible mechanism that might explain the hysteresis would involve viscoelastic behavior of the alkanethiol film. As the name suggests, a viscoelastic material exhibits both elastic and viscous properties under an applied load; it is the viscous component that gives rise to a hysteresis due to energy dissipation in the material. The amount of hysteresis (i.e., the size of the hysteresis loop) is dependent on the ratio of the relaxation time constant to the loading time.[64] For loading rates in which the data acquisition is on the order of the relaxation time constant, the hysteresis loop would be large. Joyce et al. used an interfacial force microscope to examine the mechanical relaxation of a long-chain ($n = 16$) alkanethiol on gold,[64] and in doing so, extracted an effective relaxation time constant of 0.08 s. In our experiments, the cantilever displacement was halted for several seconds as the $I-V$ measurements were performed, meaning that the alkanethiol film had sufficient time to respond to the applied load. However, it is well-known that polymers can exhibit relaxation on multiple time scales, and as a result, it is not possible to completely rule out viscoelasticity as a possible source of the observed hysteresis. Yet another possible explanation for the hysteresis is plastic deformation in the alkanethiol film. In this scenario, the monolayer exhibits both elastic and plastic deformation during loading, but only recovers elastic displacements on unloading, resulting in larger values of G on unloading. Some studies provide evidence for permanent deformation on unloading,[63] while others illustrate that sharp tips can in fact *reversibly* displace alkanethiols.[65] In light of these arguments and to simplify the subsequent analysis, we only consider the unloading portion of each $F-d$ curve, as it can be analyzed by elastic contact theory without regard to irreversibility and hysteresis.

AFM $F-\delta$ data (unloading curve only) for $n = 12$ are shown in Figure 6. $F-\delta$ data were derived from the raw $F-d$ curves by subtracting the cantilever deflection, F/k. In principle, the work of adhesion w can be found by integrating the $F-\delta$ curve, normalized by A, from z_0 to infinity.[66,67] In most AFM experiments,

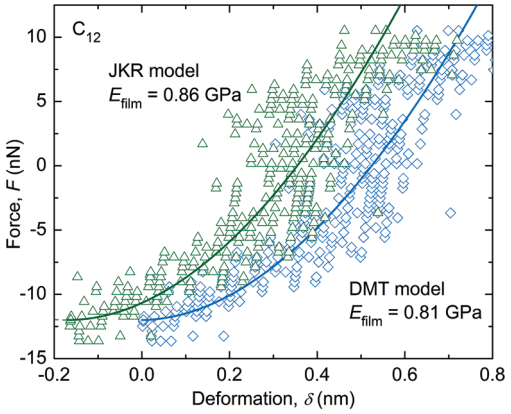

Figure 6. $F-\delta$ experimental data (symbols) and theoretical fits (solid lines) for $n = 12$. The theoretical fits are based on the extended JKR and DMT contact models, using the modulus of the film E_{film} as the fitting parameter. The experimental data are the same in each case, shifted along the horizontal axis to fit the appropriate contact model. Both the JKR and DMT models fit the $F-\delta$ data well, but with different values of w and E_{film}.

however, the snap-on and pull-off instabilities described above preclude the full $F-\delta$ curve from being collected. Thus, it becomes necessary to use the pull-off force F_{po}, in conjunction with a particular contact theory, to extract values for w. In the JKR model (eqs 1 and 2), w is related to F_{po} by $w = -F_{po}/(3/2\pi R)$, while for the DMT model (eqs 3 and 4), $w = -F_{po}/2\pi R$. To find Young's modulus of the film E_{film}, the JKR and DMT models were fit to the same set of $F-\delta$ data as shown in Figure 6, using eqs 6, 7, and 8 for the reduced modulus E^* and E_{film} as the fitting parameters. $E_{sub} = 77$ GPa and $\nu_{sub} = 0.42$ were used for the Au substrate,[68] and $\nu_{film} = 0.44$ was used for the monolayer film.[69] Both the JKR and DMT models fit the $F-\delta$ data well, but with different values of w and E_{film}. From the JKR model, we find $w = 127.3$ mJ m^{-2}, $E_{film} = 0.86$ GPa ($E^* = 7.4$ GPa at $F = 0$), and $z_0 = 0.35$ nm, which yields a Tabor parameter of $\mu = 0.52$ from eq 5. On the other hand, with the DMT model, $w = 95.5$ mJ m^{-2}, $E_{film} = 0.81$ GPa ($E^* = 5.3$ GPa at $F = 0$), and $z_0 = 0.52$ nm, which results in $\mu = 0.36$. Thus, even at modest values of F, the DMT theory is a good approximation. As F increases, E^* increases (due to substrate effects) and μ decreases, pushing our system further into the DMT zone. As a result, the DMT model was fit to the AFM $F-\delta$ data (unloading curves only) for $n = 5, 8, 12$, and 18, as shown in Figure 7. The extracted values for w and E_{film} from several measurements are given in Table 1.

For $n = 18$, we find that $w = 82.8$ mJ m^{-2}, which is in good agreement with results from bulk contact angle studies,[70] 46 mJ m^{-2} to 62 mJ m^{-2}, surface force apparatus experiments,[71] 56 mJ m^{-2}, and interfacial force microscope studies,[72] 60 mJ m^{-2}, of similar low-energy hydrocarbon molecules. The value is also consistent with results from Lifshitz theory, which indicates that the adhesion can be attributed mostly to van der Waals forces.[72,73] However, as n decreases, w increases. Berger et al. noted a similar trend with liquid-condensed (LC) and liquid-expanded (LE)

(62) Schneider, J.; Dori, Y.; Haverstick, K.; Tirrell, M.; Sharma, R. *Langmuir* **2002**, *18*, 2702.
(63) Engelkes, V. B.; Frisbie, C. D. *J. Phys. Chem. B* **2006**, *110*, 10011.
(64) Joyce, S. A.; Thomas, R. C.; Houston, J. E.; Michalske, T. A.; Crooks, R. M. *Phys. Rev. Lett.* **1992**, *68*, 2790.
(65) Liu, G.; Salmeron, M. B. *Langmuir* **1994**, *10*, 367.
(66) DelRio, F. W.; de Boer, M. P.; Knapp, J. A.; Reedy, E. D.; Clews, P. J.; Dunn, M. L. *Nat. Mater.* **2005**, *4*, 629.
(67) DelRio, F. W.; Dunn, M. L.; de Boer, M. P. *Scr. Mater.* **2008**, *59*, 916.
(68) Callister, W. D. *Materials Science and Engineering: An Introduction*; John Wiley and Sons: New York, 2000.
(69) Wang, M.; Liechti, K. M.; Srinivasan, V.; White, J. M.; Rossky, P. J.; Stone, M. T. *J. Appl. Mech.* **2006**, *73*, 769.
(70) Zisman, W. A.; Fox, H. W. *J. Colloid Sci.* **1952**, *7*, 428.
(71) Israelachvili, J. N. *J. Vac. Sci. Technol.* **1992**, *A10*, 2961.
(72) Thomas, R. C.; Houston, J. E.; Crooks, R. M.; Kim, T.; Michalske, T. A. *J. Am. Chem. Soc.* **1995**, *117*, 3830.
(73) Israelachvili, J. *Intermolecular and Surface Forces*; Academic Press: London, 1992.

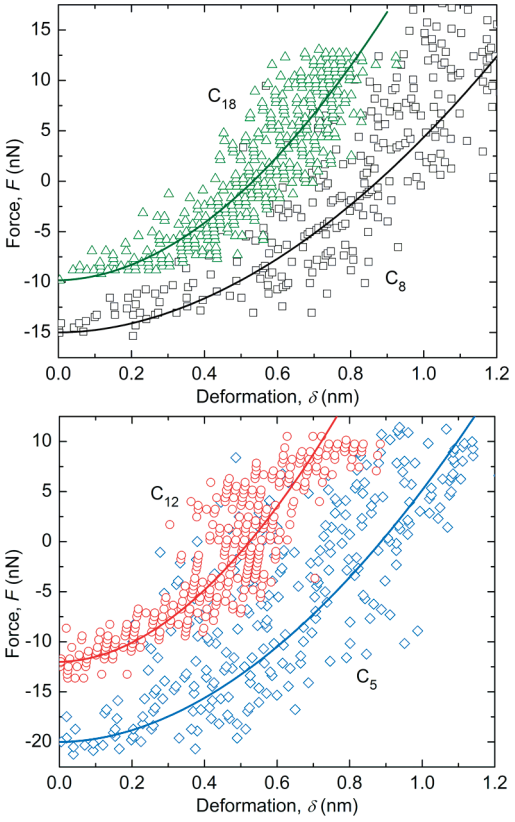

Figure 7. $F-\delta$ experimental data (symbols) and theoretical fits (solid lines) for $n = 5, 8, 12$, and 18. The theoretical fits are based on the extended DMT contact model, using the modulus of the film E_{film} as the fitting parameter. The DMT theory is a good approximation, even at modest values of F, according to the calculated values for μ.

domains in a phase-separated lipid monolayer.[74] The change was attributed to differences in molecular orientation and order: in the LC domains, the molecules were densely packed, and the probe tip interacted only with the CH_3 end groups, whereas in the LE domains, the films were liquid-like, and the adhesion was mainly due to CH_2 groups along the hydrocarbon chain. With $\gamma_{CH2} = 31\ mJ\ m^{-2}$ and $\gamma_{CH3} = 23\ mJ\ m^{-2}$, $w_{CH2}/w_{CH3} = (\gamma_{CH2}/\gamma_{CH3})^{1/2} = 1.2$, where γ_a and w_a are the surface energy and work of adhesion for molecule a, respectively. Seeing as the average tilt angle increases as n decreases, as shown by the trends in R_I, a similar increase in work of adhesion should be expected here due to the additional CH_2 groups at the surface. However, the increase in adhesion goes beyond a simple CH_3 versus CH_2 argument, as evident from $w_{C5}/w_{C18} = 2.0$. Koleske et al. showed that the elastic modulus of a film may also affect tip−surface interactions.[75] From Table 1, it is clear that E_{film} decreases from 1.0 to 0.15 GPa as n decreases from 18 to 5. As E_{film} decreases, δ at a given F increases, exposing the tip to additional functional groups in the film or to the substrate. Thus, for the short-chain molecules, we would expect an increase in w, as the tip is closer to the substrate and the Hamaker constant for metals is an order of magnitude greater than that for hydrocarbons.[73]

The variation of E_{film} with n can be divided into three regions, each the result of a different variation mechanism, but which all derive from the variation of the attractive van der Waals

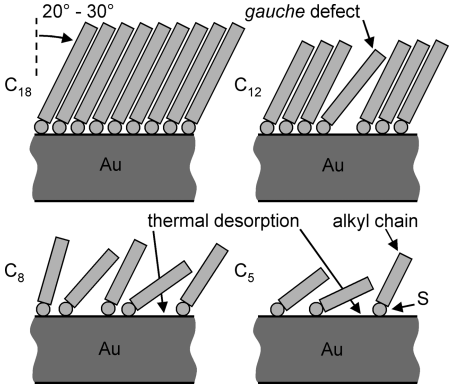

Figure 8. Schematic diagrams of alkanethiol monolayers with different n. For $n = 18$, the alkyl chains form a densely packed, crystalline-like film with an *average* tilt angle of 20° to 30° to the surface normal. As n decreases, there is an increase in the tilt angle followed by a change in phase from crystalline to amorphous and a loss in surface coverage due to thermal desorption.

interactions between alkyl chains with n.[76] As n increases for densely packed chains, the stabilization energy provided by additional CH_2 groups decreases, and eventually saturates at $n \approx 10$. Hence, the small decrease in E_{film} as n decreased from 18 to 12 arises from a small decrease in molecular stability. This decrease in stability gives rise to an increase in the concentration of *gauche* defects in the topmost methyl unit[77] as shown in Figure 8. The defects increase the *average* tilt angle of the alkyl chains, which is evident from the decrease in R_I. For n decreasing from 12 to 8, E_{film} decreased by an additional factor of 3. In this range, the intermolecular forces are no longer invariant with n, but decrease drastically as n decreases, resulting in a greater number of *gauche* defects. As a consequence, there is a change in phase from crystalline to amorphous ($R_I \rightarrow 0$), which reduces the film's resistance to elastic deformation. For $n < 8$, a lack of cohesive energy leads to thermal desorption of the alkyl chains,[78] and the loss of surface coverage leads to the decrease in E_{film} over this range. The variation mechanisms above are consistent with the NEXAFS data in Figure 4 and Table 1, which also point to an increase in molecular tilt relative to the normal followed by a change in phase and a loss in surface coverage for decreasing n.

Overall, the results for E_{film} are in agreement with a number of previous studies for both bulk polyethylene and alkanethiol monolayers. For instance, the values for the short-chain ($n = 5$ and 8) and long-chain ($n = 12$ and 18) molecules are consistent with results for low-density (0.17 to 0.28 GPa) and high-density (1.08 GPa) polyethylene, respectively.[68] Tensile testing of oriented high-density polyethylene revealed a Young's modulus of 0.80 GPa for as-fabricated samples and moduli as large as 3.05 GPa for samples with a significant amount of plastic deformation, with the increase presumably due to strain-induced crystallization (i.e., an increase in overall crystallinity).[79] While the initial value for the elastic modulus is consistent with our results, an increase in modulus from permanent deformation would not be expected here, as alkanethiol monolayers become disordered, not ordered, at pressures of ~0.8 GPa.[65] A number of scanning probe microscopy experiments have also suggested that E_{film} for long-chain

(74) Berger, C. E. H.; van der Werf, K. O.; Kooyman, R. P. H.; de Grooth, B. G.; Greve, J. *Langmuir* **1995**, *11*, 4188.
(75) Koleske, D. D.; Barger, W. R.; Lee, G. U.; Colton, R. *J. Mater. Res. Soc. Proc.* **1997**, *464*, 377.
(76) Xiao, X.; Hu, J.; Charych, D. H.; Salmeron, M. *Langmuir* **1996**, *12*, 235.
(77) Hautman, J.; Klein, M. L. *J. Chem. Phys.* **1989**, *91*, 4994.
(78) Nuzzo, R. G.; Zegarski, B. R.; Dubois, L. H. *J. Am. Chem. Soc.* **1987**, *109*, 733.
(79) Bartczak, Z.; Morawiec, J.; Galeski, A. *J. Appl. Polym. Sci.* **2002**, *86*, 1405.

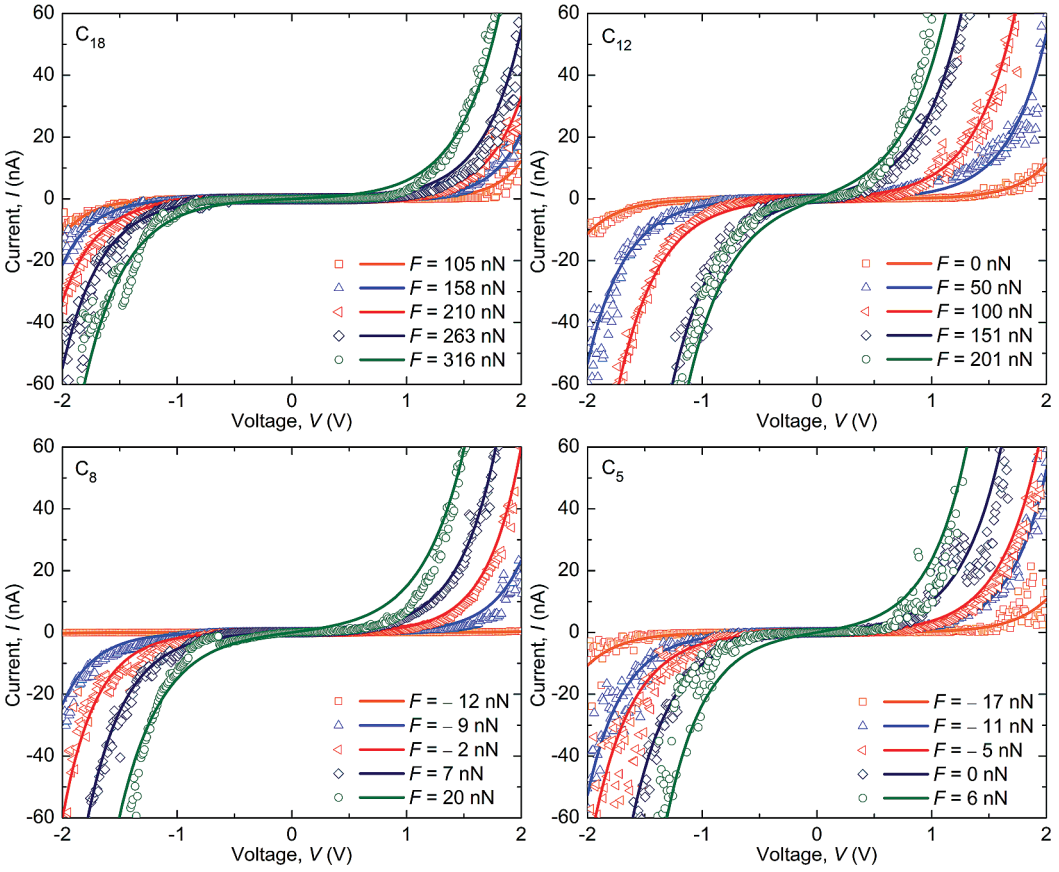

Figure 9. $I-V$ responses for $n = 5, 8, 12$, and 18. The symbols represent measurements for a single voltage sweep; the solid lines represent best fits to the data using a parabolic-barrier tunneling model, with $\phi_0 - E_F$ and t as the fitting parameters.

($n > 10$) alkanethiol monolayers is between 0.1 and 5 GPa.[80−83] In addition, molecular dynamics simulations of similar organic monolayers demonstrated an initial tangent modulus of 1.5 GPa.[69]

Other studies, however, report much greater moduli for organic monolayers, from 15 to 75 GPa. For instance, Engelkes and Frisbie conducted low-bias conductance measurements of various alkanethiol monolayers as a function of applied load.[63] The conductance data were analyzed with the DMT contact model and tunneling equations to extract the reduced film modulus. The results showed a decrease in modulus (54 to 48 GPa) with increasing chain length for $n = 6$, 8, and 10, followed by an increase in modulus (75 GPa) for $n = 12$. In the analysis, the moduli were extracted based on the assumption that the measured properties were free from substrate effects. However, as the contact depths were often on the order of the film thicknesses, the underlying substrate most likely played a role, and therefore must be considered to determine the true film properties. To illustrate the role of the substrate, we again fit the DMT model to the AFM $F-\delta$ data in Figure 7, this time assuming $E^* = E_{film}/(1 - \nu_{film}^2)$ instead of using eqs 6, 7, and 8. In this revised approach, the extracted values for E_{film} varied from 3.9 to 5.5 GPa, with no observable trend between E_{film} and n. Consequently, by neglecting the substrate, the calculated properties are almost an order of magnitude greater than the true film properties. In another study, Henda et al. utilized a static energy minimization technique to examine the elastic response of alkanethiol monolayers under compression.[84] The calculations showed that the initial tangent moduli of the monolayers were between 10 and 18 GPa, with the values nearly independent of n. The moduli were extracted based on the assumption that the film was in uniaxial compression. However, as periodic boundary conditions were used, the periphery of the film was constrained, and the stress state was in fact triaxial.[69] As a result, the reported values for E_{film} were inflated by a factor of $(1 - \nu_{film})/(1 - 2\nu_{film})$-$(1 + \nu_{film})$.

Charge Transport Properties. AFM $I-V$ traces (recorded during the unloading portions of the $F-\delta$ curves only) for $n = 5$, 8, 12, and 18 are shown in Figure 9. For all values of n, $I-V$ behavior was strongly dependent on contact load, with increased F leading to increased G. In addition, the $I-V$ responses were non-Ohmic, symmetric about zero bias, with conductance values smaller than G_0, which suggests that charge transport involved electron tunneling through an insulating layer. Thus, it becomes necessary to use an electron tunneling model appropriate for ultrathin insulating layers (eqs 9, 10 and 11) to relate the $I-V$ behavior to a, in conjunction with the DMT contact theory (eqs 3 and 4) to describe the variation of a with F, to correlate the $I-V$ data to F. As shown in Figure 9, the parabolic tunneling model (solid lines) was fit to the experimental data (symbols) with good agreement, using $\phi_0 - E_F$ and t as the fitting parameters. The resulting values for $\phi_0 - E_F$ and t are shown in Figure 10.

For all n, we find that the extracted results for $\phi_0 - E_F$ are effectively independent of F, as there are no clear trends, and the

(80) Salmeron, M.; Neubauer, G.; Folch, A.; Tomitori, M.; Ogletree, D. F.; Sautet, P. *Langmuir* **1993**, *9*, 3600.
(81) Kiridena, W.; Jain, V.; Kuo, P. K.; Liu, G. *Surf. Interface Anal.* **1997**, *25*, 383.
(82) Houston, J. E.; Kim, H. I. *Acc. Chem. Res.* **2002**, *35*, 547.
(83) Price, W. J.; Leigh, S. A.; Hsu, S. M.; Patten, T. E.; Liu, G. *J. Phys. Chem. A* **2006**, *110*, 1382.

(84) Henda, R.; Grunze, M.; Pertsin, A. J. *Trib. Lett.* **1998**, *5*, 191.

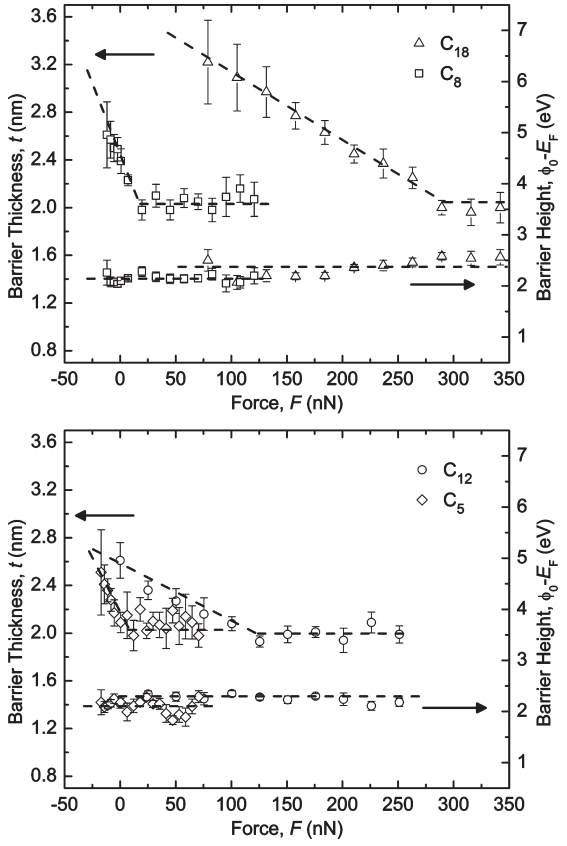

Figure 10. $\phi_0 - E_F$ (right) and t (left) as a function of F for $n = 5, 8$, 12, and 18. For all n, the extracted results for $\phi_0 - E_F$ are effectively independent of F. The variations in t with F can be divided into two regions. One possible explanation for the change in behavior involves the presence of *two* insulating layers: an oxide layer on the Co−Cr tip and the alkanethiol monolayer on the Au surface.

average values (represented by dashed lines in Figure 10 and numerically in Table 1) typically fall within the uncertainty of measured values. The results for $\phi_0 - E_F$ are in good agreement with previously reported values for alkanethiols, which range from 1.4 to 2.9 eV.[47,85−89] From Table 1, it appears as if the barrier height might be chain length dependent; as n decreases from 18 to 5, $\phi_0 - E_F$ decreases from 2.4 to 2.1 eV. In fact, using Student's t test, we find that the difference for $n = 18$ and 12 is significant at the 95% level, while the differences for $n = 12$ and 8 and $n = 8$ and 5 are significant at the 85% level. There are two possible reasons for a variation in $\phi_0 - E_F$: (1) a change in E_F or (2) a change in the HOMO−LUMO energy gap. On the first point, the Fermi energy is expected to remain constant as a function of n, as the same AFM tip and substrate were used in all of the experiments. On the second point, Boulas et al. conducted photoconductivity experiments at variable excitation wavelengths to extract the HOMO−LUMO energy gaps for several long-chain ($n = 12$, 16, and 18) alkyl-based monolayers.[23] The HOMO−LUMO gap was found to be independent of n, with values ranging from 9.2 to 9.9 eV. As a result, for densely packed, crystalline-like

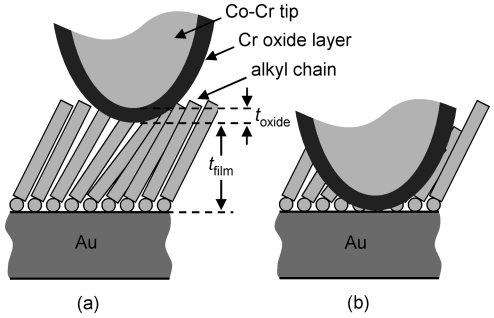

Figure 11. Schematic diagrams of the Co−Cr tip in contact with the alkanethiol monolayer. At small F, the alkanethiol film and oxide layer both act as insulators, $t = t_{film} + t_{oxide}$. At large F, however, the alkanethiol film is compressed and the oxide layer is the sole interlayer, $t = t_{oxide}$.

films, $\phi_0 - E_F$ should be independent of n. However, by changing the deposition conditions, the authors were also able to examine some of the same films in a liquid-like state with only partial surface coverage. The resulting photocurrent curves were shifted toward smaller barrier heights, which yields a large decrease (> 1 eV) in the HOMO−LUMO energy gap. Thus, it was shown that a *qualitative* relationship exists between the molecular orientation, order, and coverage and the barrier height, presumably due to changes in the free volume between the chains. Here, we arrive at the same conclusion, and provide *quantitative* evidence for the link between film structure and transport properties; as n decreases, both R_I and $\phi_0 - E_F$ decrease. This effect has been attributed to image charges generated in the metal electrodes by trapped charges in the molecule, which leads to a localization of charge at the metal−molecule interface and a significant change in the intrinsic energy levels.[90] However, other studies suggest that $\phi_0 - E_F$ is constant for alkanethiols, regardless of the molecular orientation and surface coverage. Beebe et al. used conducting-probe AFM and crossed-wire tunnel junctions to investigate the effect of n on the voltage required to induce a transition from direct tunneling to field emission, denoted by V_{trans}.[91,92] V_{trans} was found to scale linearly with $\phi_0 - E_F$ for π-conjugated thiol monolayers using ultraviolet photoelectron spectroscopy.[91] For both short-chain and long-chain alkanethiol films, V_{trans} was constant,[92] which led to the conclusion that $\phi_0 - E_F$ was independent of n.

The variations in t with F can be divided into two regions for all n; at small F, t decreases monotonically, while at large F, t remains constant. One possible explanation for the change in behavior involves the presence of *two* insulating layers: an oxide layer (thickness t_{oxide}) on the Co−Cr tip, and the alkanethiol monolayer (thickness t_{film}) on the Au surface, as shown in Figure 11. In this scenario, the probe tip compresses the compliant alkanethiol monolayer during the initial stages of contact. Eventually, the alkanethiol layer is compressed between the contacts, and the insulating layer consists mainly of the oxide layer on the Cr surface, which is more difficult to deform. Chromium thin films are known to readily form native oxide layers under ambient conditions; the standard enthalpy of formation for Cr_2O_3, for example, is $\Delta H^0_f = -1140$ kJ mol^{-1}.[93] In one study, the thickness

(85) Wold, D. J.; Frisbie, C. D. *J. Am. Chem. Soc.* **2001**, *123*, 5549.
(86) Holmlin, R. E.; Haag, R.; Chabinyc, M. L.; Ismagilov, R. F.; Cohen, A. E.; Terfort, A.; Rampi, A.; Whitesides, G. M. *J. Am. Chem. Soc.* **2001**, *123*, 5075.
(87) Fan, F. R. F.; Yang, J.; Cai, L.; Price, D. W.; Dirk, S. M.; Kosynkin, D. V.; Yao, Y.; Rawlett, A. M.; Tour, J. M.; Bard, A. J. *J. Am. Chem. Soc.* **2002**, *124*, 5550.
(88) Cui, X. D.; Zarate, X.; Tomfohr, J.; Sankey, O. F.; Primak, A.; Moore, A. L.; Moore, T. A.; Gust, D.; Harris, G.; Lindsay, S. M. *Nanotechnology* **2002**, *13*, 5.
(89) Lee, T.; Wang, W.; Klemic, J. F.; Zhang, J. J.; Su, J.; Reed, M. A. *J. Phys. Chem. B* **2004**, *108*, 8742.
(90) Kubatkin, S.; Danilov, A.; Hjort, M.; Cornil, J.; Brédas, J. −L.; Stuhr-Hansen, N.; Hedegard, P.; Bjørnholm, T. *Nature* **2003**, *425*, 698.
(91) Beebe, J. M.; Kim, B.; Gadzuk, J. W.; Frisbie, C. D.; Kushmerick, J. G. *Phys. Rev. Lett.* **2006**, *97*, 026801.
(92) Beebe, J. M.; Kim, B.; Frisbie, C. D.; Kushmerick, J. G. *ACS Nano* **2008**, *2*, 827.
(93) Aylward, G. H.; Findlay, T. J. V. *SI Chemical Data*; John Wiley: Sydney, 1974.

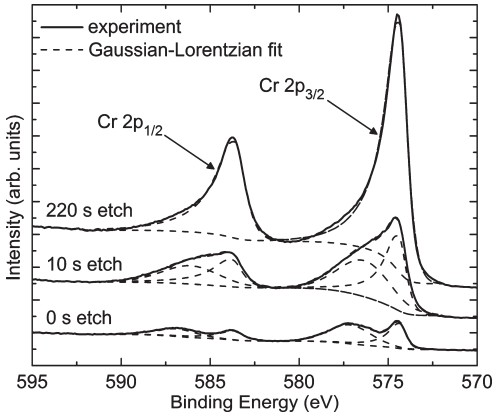

Figure 12. XPS Cr 2p spectra for sputter times of 0 s, 10 s, and 220 s (offset for clarity). The elemental Cr peaks are at ~574.4 and 583.6 eV, while the Cr_2O_3 peaks are at ~576.5 and 586.3 eV. After 10 s, the adventitious C (not shown here) was reduced to 35% of its initial value, and the signals for elemental Cr and Cr_2O_3 increased by factors of 3.7 and 2.4, respectively. After 220 s, the Cr_2O_3 peaks were no longer detectable.

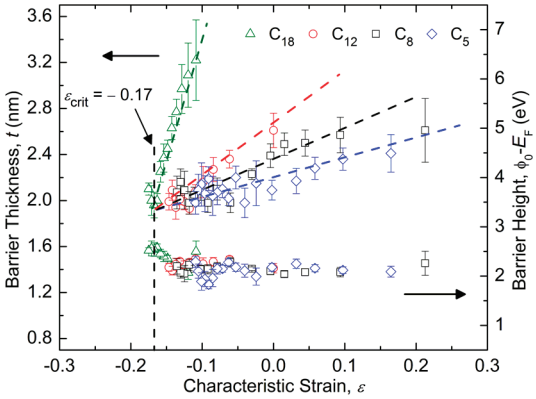

Figure 13. $\phi_0 - E_F$ (right) and t (left) as a function of ε for $n = 5, 8, 12$, and 18. For positive ε, $\phi_0 - E_F$ is constant at 2.1 eV, but as ε decreases, $\phi_0 - E_F$ increases to 2.6 eV. The critical strain ε_{crit}, or the strain required to displace the film, is shown to be $\varepsilon_{crit} = -0.17$.

of the oxide layer varied from 2 to 6 nm, with values depending on the thickness of the chromium film and the underlying substrate material.[94] To estimate t_{oxide} on our AFM cantilever, the cantilever surface was sputtered and XPS high resolution region scans were performed initially every 10 s and then at 20 s intervals throughout the sputter etch. Figure 12 shows the Cr 2p region for sputtering times of 0, 10, and 220 s. After 10 s, the adventitious C (not shown here) was reduced to 35% of its initial value, and the signals for elemental Cr and Cr_2O_3 increased by factors of 3.7 and 2.4, respectively. In subsequent sputter steps, the elemental Cr peak monotonically increased, while the Cr_2O_3 peak increased another 5% after 20 s and then decreased steadily until it was no longer detectable after 220 s. Subsequent sputtering did not result in increased signal for the elemental Cr peak. The elemental Cr $2p_{3/2}$ peaks were fit with 30% Gaussian−70% Lorentzian peaks with an exponential blend parameter of 0.8, while the Cr $2p_{3/2}$ peaks for Cr_2O_3 were fit with 70% Gaussian−30% Lorentzian peaks. With these spectra, t_{oxide} was calculated using a standard uniform overlayer model[95] $I_{Cr} = I^0_{Cr} \exp(-t_{oxide}/L_{Cr})$, where the initial value of Cr, I_{Cr}, was the peak area for the elemental Cr $2p_{3/2}$ of the unsputtered sample, and the final base value, I^0_{Cr}, was an average of the elemental Cr $2p_{3/2}$ peak areas for 260, 280, and 300 s sputter times. NIST Standard Reference Database 82 was used to calculate the practical effective attenuation length[96] L_{Cr} for elemental Cr electrons passing through a Cr_2O_3 overlayer. The calculations were based on the kinetic energy of the base electrons $KE = 912.5$ eV, asymmetry parameter $\beta = 1.45$, and the following Cr_2O_3 parameters: band gap energy[97] of 3.7 eV and density[98] of 5250 kg m^{-3}. This calculation resulted in a Cr_2O_3 thickness of 3.9 nm. However, as the adventitious C on the surface also contributed to the attenuation, 3.9 nm can be viewed as an upper bound on the Cr_2O_3 thickness. To determine a lower bound for t_{oxide}, the Cr_2O_3 thickness was recalculated with I_{Cr} as the elemental Cr $2p_{3/2}$ peak area after 10 s of sputtering. At this depth, most of the C was etched from the surface, in addition to some of the Cr_2O_3 layer, as evident by the increase in the Cr/Cr_2O_3 signal ratio. This second estimate resulted in a Cr_2O_3 thickness of 1.9 nm. Hence, the XPS results indicate that t_{oxide} was between 1.9 and 3.9 nm. From this analysis, it seems reasonable to assume that the constant values for t at large F, which are all around 2.2 nm as shown in Figure 10, are due to an oxide layer on the Co−Cr tip.

As the tip was retracted from the surface, elastic displacements were eventually recovered from the alkanethiol monolayer, and the extracted values for $t = t_{film} + t_{oxide}$, as shown in Figure 11. This observation raises a key point about the mechanical and electrical behavior of the oxide layer on the Co−Cr tip. From a mechanical standpoint, the modulus of the oxide layer E_{oxide} is much greater than the modulus of the alkanethiol film E_{film}, and, as a result, the deformation of the oxide layer δ_{oxide} will represent only a small portion of the total deformation at the contact δ. Thus, t in eqs 6, 7, and 8 is just the monolayer thickness, i.e., $t = t_{film}$, and does not depend on the oxide layer. With an applied voltage, however, the alkanethiol film and the oxide layer both act as insulators, and as mentioned above, t is a function of both t_{film} and t_{oxide}. Therefore, to get t_{film} as a function of F in Figure 10, t_{oxide} must be subtracted according to $t_{film} = t - t_{oxide}$. For all n, (1) t_{film} increases monotonically as F decreases and (2) t_{film} at $F = 0$ is less than the original film thickness, due to elastic recovery and viscoelastic−plastic deformation, respectively. The average values for the viscoelastic−plastic deformation δ_p, or the difference between t_{film} at $F = 0$ and the original film thickness, are shown in Table 1. While δ_p is fairly constant for all n except $n = 12$, it is difficult to draw any definite conclusions about the relationship between δ_p and n at a given F, since the maximum F in each experiment in Figure 10 was different.

It is possible, however, to "normalize" the data in Figure 10 by plotting $\phi_0 - E_F$ and t as a function of a characteristic strain $\varepsilon = F/AE^*$ as shown in Figure 13. In doing so, two distinct features become clear, both of which are independent of n. First, $\phi_0 - E_F$ is strain-dependent; for positive (tensile) ε, $\phi_0 - E_F$ is constant at ~2.1 eV, but as ε decreases into negative (compressive) values, $\phi_0 - E_F$ increases to almost 2.6 eV. Slowinski et al.[99] and later Song et al.[100] showed that the dominant charge transport mechanism for alkanethiols transitions from through-bond tunneling,

(94) Matyi, R. J.; Hatzistergos, M. S.; Lifshin, E. *Thin Solid Films* **2006**, *515*, 1286.
(95) Petrovykh, D. Y.; Kimura-Suda, H.; Tarlov, M. J.; Whitman, L. J. *Langmuir* **2004**, 20 429.
(96) Powell, C. J.; Jablonski, A. *NIST Electron Effective-Attenuation-Length Database - Version 1.1*; National Institute of Standards and Technology: Gaithersburg, MD, 2003.
(97) Tsuchiya, H.; Fujimoto, S.; Chihara, O.; Shibata, T. *Electrochim. Acta* **2002**, *47*, 4357.
(98) Gasgnier, M.; Nevot, L. *Phys. Status Solidi* **1981**, *66*, 525.
(99) Slowinski, K.; Chamberlain, R. V.; Miller, C. J.; Majda, M. *J. Am. Chem. Soc.* **1997**, *119*, 11910.
(100) Song, H.; Lee, H.; Lee, T. *J. Am. Chem. Soc.* **2007**, *129*, 3806.

where electrons flow through the alkyl chains via overlapping σ-bonds, to chain-to-chain coupling, which involves charge transfer between adjacent hydrocarbon chains, as the tilt angle increases. In fitting the data to the two-pathway model, the authors demonstrated that the tunneling decay coefficient, defined as the change in junction resistance at low-bias with n, for chain-to-chain tunneling is greater than that for through-bond tunneling. In other words, chain-to-chain coupling is less efficient for charge transport, but becomes significant at large tilt angles, which is consistent with the increase in $\phi_0 - E_F$ at negative ε in Figure 13. Second, while the rate at which t changes with ε is dependent on n (due to the variations in E_{film} as shown in Table 1), the strain at which the film is completely displaced from under the tip is not. From Figure 13, this critical strain ε_{crit} is shown to be $\varepsilon_{crit} = -0.17$, which might represent the strain required to change the sulfur−gold binding structure (e.g., shift a sulfur atom from a hollow site to a bridge site on the gold) to accommodate large tilt angles.[19]

Summary and Conclusions

In summary, the mechanical and electrical properties of alkanethiol monolayers on gold were examined with AFM and correlated with surface structure via NEXAFS. AFM contact data were analyzed with the DMT contact model, modified to extract the film modulus by a first-order elastic perturbation method to account for substrate effects, and a parabolic tunneling-barrier conductance model, appropriate for a metal−insulator−metal contact in which the insulator is extremely thin. NEXAFS carbon K-edge spectra were used to compute R_I for each film, which provided a quantitative measure of the molecular structure as a function of n.

As n decreased from 18 to 5, there was a change in phase from crystalline to amorphous ($R_I \rightarrow 0$) and loss of surface coverage (intensity of the C=C π^* resonance peak increased), which resulted in the following trends in the film properties:

(1) w increased from 82.8 mJ m^{-2} to 168.3 mJ m^{-2}. As n decreased, the ratio of CH_2 to CH_3 groups under the tip increased, and as a result, w increased according to $w_{CH2}/w_{CH3} = 1.2$. Also, for the short-chain molecules, w increased because the tip was closer to the substrate at a given F, and the Hamaker constant for the gold substrate is roughly an order of magnitude greater than that for the hydrocarbon chains.

(2) E_{film} decreased from 1.0 to 0.15 GPa. The change in E_{film} with n was due to variations in the attractive van der Waals interactions between alkyl chains. As n increased, the stabilization energy provided by additional CH_2 groups decreased, and eventually saturated at $n \approx 10$.

(3) $\phi_0 - E_F$ decreased from 2.4 to 2.1 eV. There were two possible explanations for the variation in $\phi_0 - E_F$: a change in E_F or a change in the HOMO−LUMO energy gap. While E_F was expected to remain constant as a function of n, a large decrease in the HOMO−LUMO energy gap was previously reported for loosely packed, liquid-like films.[23]

For all n, the variations in t with F were divided into two regions; at small F, t decreased monotonically, while at large F, t remained constant at about 2.2 nm. One possible explanation for the change in behavior involved the presence of *two* insulating layers: an oxide layer on the Co−Cr tip and the alkanethiol monolayer on the Au surface. XPS confirmed the presence of an oxide layer on the Co−Cr tip, and by sputtering the surface and performing high resolution region scans throughout the thickness, it was shown that t_{oxide} is between 1.9 and 3.9 nm. Finally, by plotting $\phi_0 - E_F$ and t as a function of ε, two distinct features were clear:

(1) $\phi_0 - E_F$ was strain-dependent; for positive ε, $\phi_0 - E_F$ was ~2.1 eV, but as ε decreased into negative values, $\phi_0 - E_F$ increased to almost 2.6 eV. For negative (compressive) values of ε, the average tilt angle increased, changing the dominant charge transport mechanism from through-bond tunneling to chain-to-chain coupling. Chain-to-chain coupling is a less efficient charge transport mechanism, which translates to larger values of $\phi_0 - E_F$.

(2) ε_{crit}, or the strain at which the film was completely displaced from under the tip, was constant at −0.17. This value might signify the strain required to change the sulfur−gold binding structure to accommodate large tilt angles.

Acknowledgment. The authors would like to thank Lee Richter and Nhan Nguyen for their assistance with the goniometry and spectroscopic ellipsometry. Certain commercial equipment, instruments, or materials are identified in this report in order to specify the experimental procedure adequately. Such identification is not intended to imply recommendation or endorsement by the National Institute of Standards and Technology, nor is it intended to imply that the materials or equipment identified are necessarily the best available for the purpose.